Science Advances
AAAS

advances.sciencemag.org/cgi/content/full/7/28/eabg0633/DC1

Supplementary Materials for

Efficient and stable inverted perovskite solar cells with very high fill factors via incorporation of star-shaped polymer

Qi Cao, Yongjiang Li, Hong Zhang, Jiabao Yang, Jian Han, Ting Xu, Shuangjie Wang, Zishuai Wang, Bingyu Gao, Junsong Zhao, Xiaoqiang Li, Xiaoyan Ma, Shaik Mohammed Zakeeruddin, Wei E. I. Sha, Xuanhua Li*, Michael Grätzel*

*Corresponding author. Email: michael.graetzel@epfl.ch (M.G.); lixh32@nwpu.edu.cn (X.L.)

Published 7 July 2021, *Sci. Adv.* **7**, eabg0633 (2021)
DOI: 10.1126/sciadv.abg0633

The PDF file includes:

Other Supplementary Material for this manuscript includes the following:

(available at advances.sciencemag.org/cgi/content/full/7/28/eabg0633/DC1)

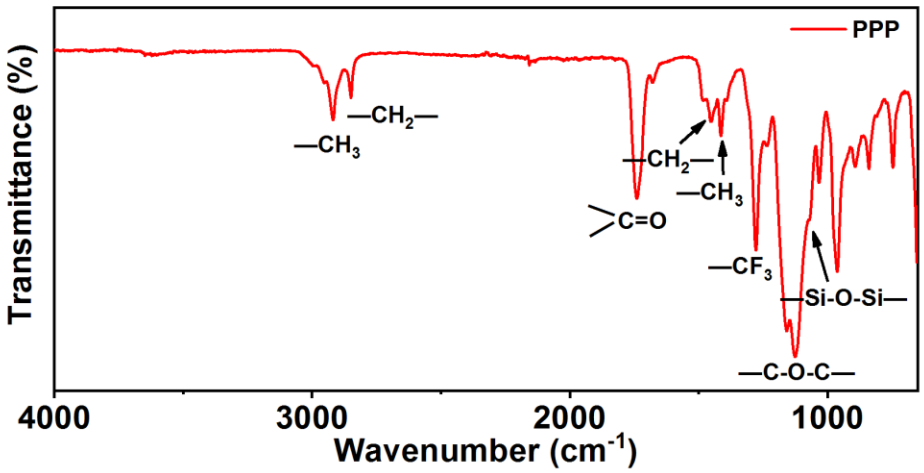

Fig. S1. FT-IR spectrum of the PPP polymer.

The FT-IR spectrum shows the appearances of peaks at 1068, 1741, and 2918 cm^{-1} which are consistent with stretching vibration of Si–O–Si, C=O, and $–CH_3$ on chain. Meanwhile, the 1453 cm^{-1} band is assigned to $–CH_2–$ scissor vibration and 1413 cm^{-1} absorption band belongs to the $–CH_3$ flexural vibration. The absorption peaks of C–O–C stretching vibration is observed at 1128 cm^{-1}. There is a peak appeared at 1277 cm^{-1} which corresponds to the C–F group of the poly (trifluoroethyl methacrylate) block.

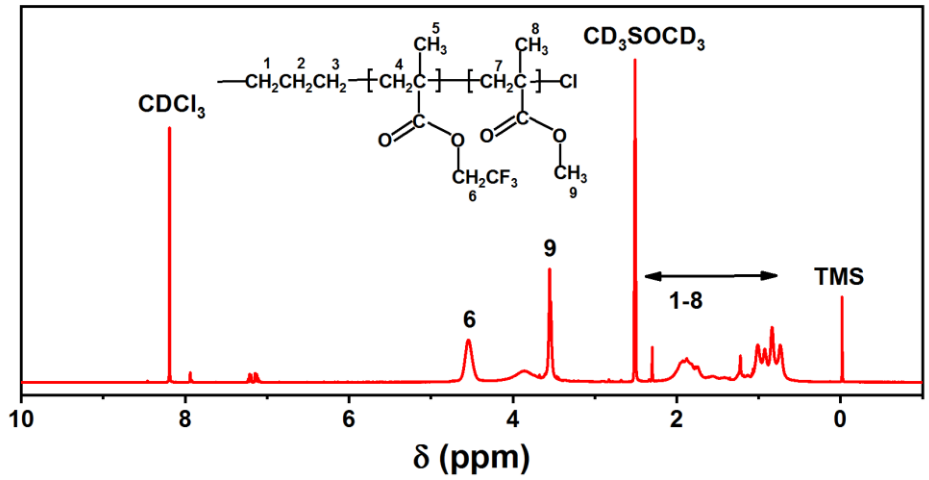

Fig. S2. ^{1}H-NMR spectroscopy of the PPP polymer. Tetramethylsilane (TMS) as an internal reference, and dimethyl sulfoxide-d_6 (CD_3SOCD_3) and chloroform-d_3 ($CDCl_3$) as mixed solvent.

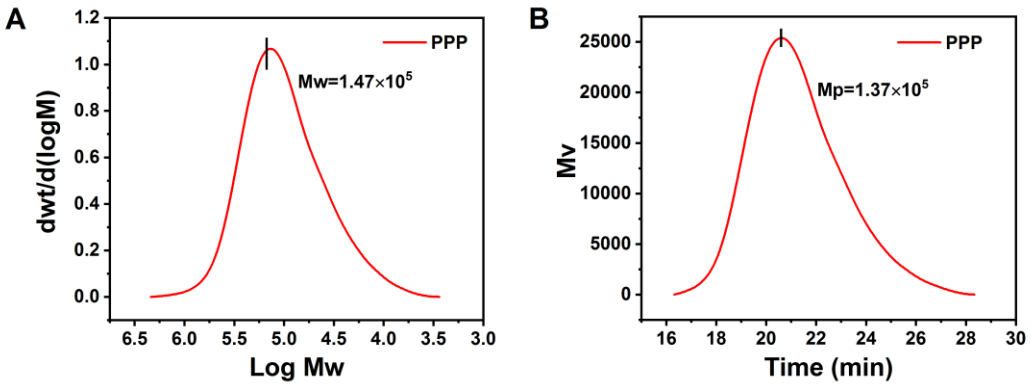

Fig. S3. The molecular weight and the molecular distribution of the PPP polymer. (**A**), Mass-average molecular weight (Mw), and (**B**), Peak molecular weight (Mp) of the PPP polymer measured by GPC.

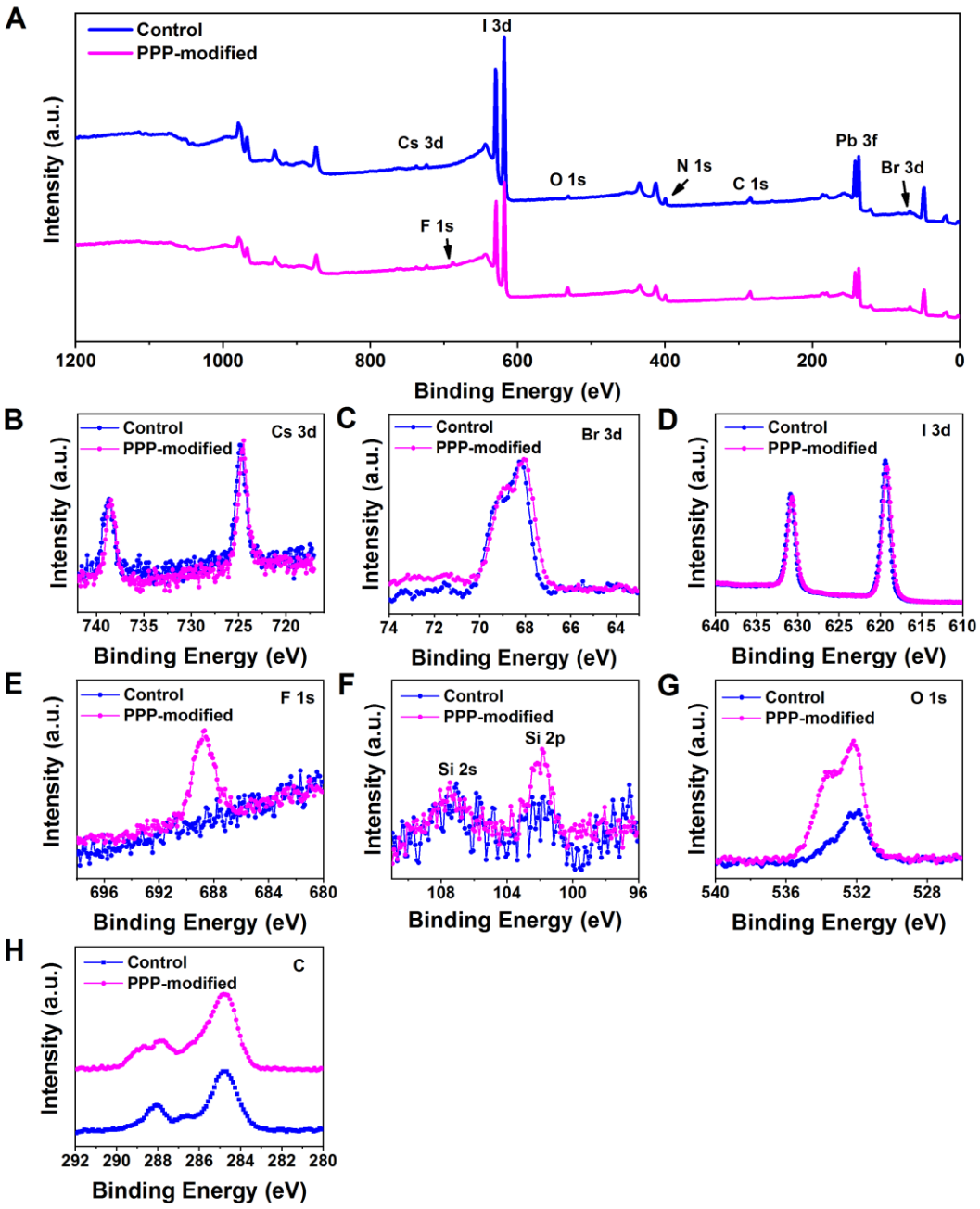

Fig. S4. Characterization of the element states of the perovskite surface with the control and PPP-modified. (**A**), XPS full spectra of the control and PPP-modified perovskite films. XPS spectra of (**B**), Cs 3*d*, (**C**), Br 3*d*, (**D**), I 3*d*, (**E**), F 1*s*, (**F**), Si, (**G**), O 1*s*, and (**H**), C for the control and PPP-modified perovskite films.

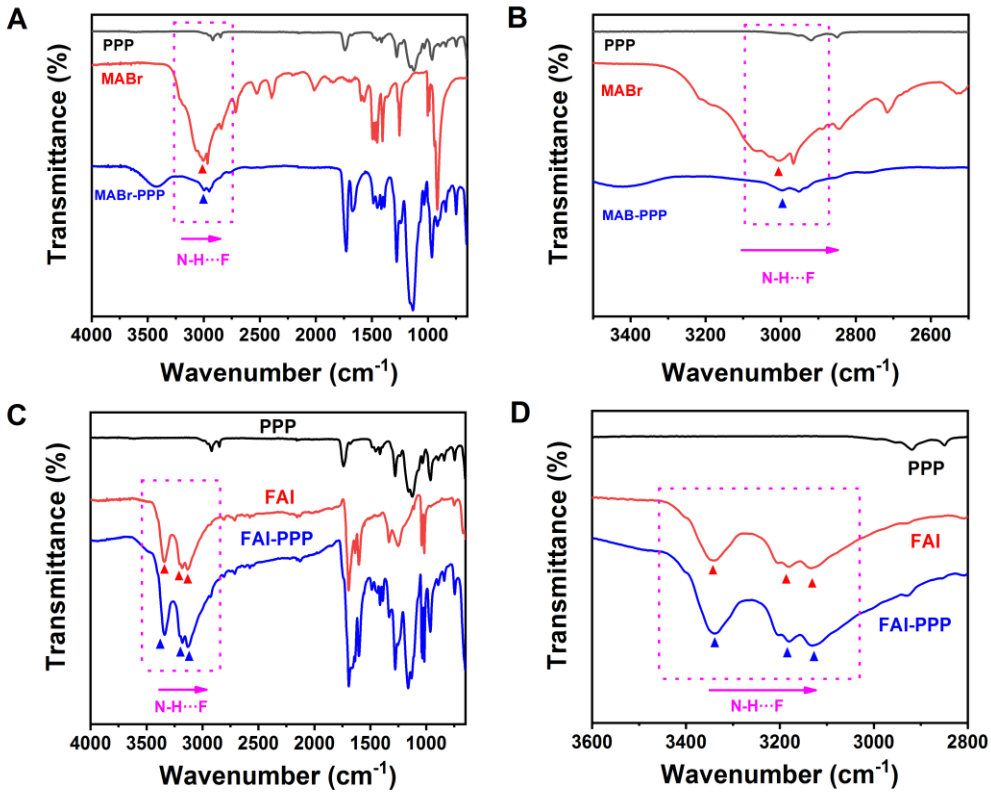

Fig. S5. Interactions between MABr, FAI and the PPP polymer. (**A**), FT-IR spectra of the PPP polymer, MABr, and PPP-MABr. (**B**), The FT-IR of the N–H stretch in MA^+. (**C**), FT-IR spectra of the PPP polymer, FAI, and PPP-FAI; (**D**), The FT-IR of the N–H stretch in FA^+.

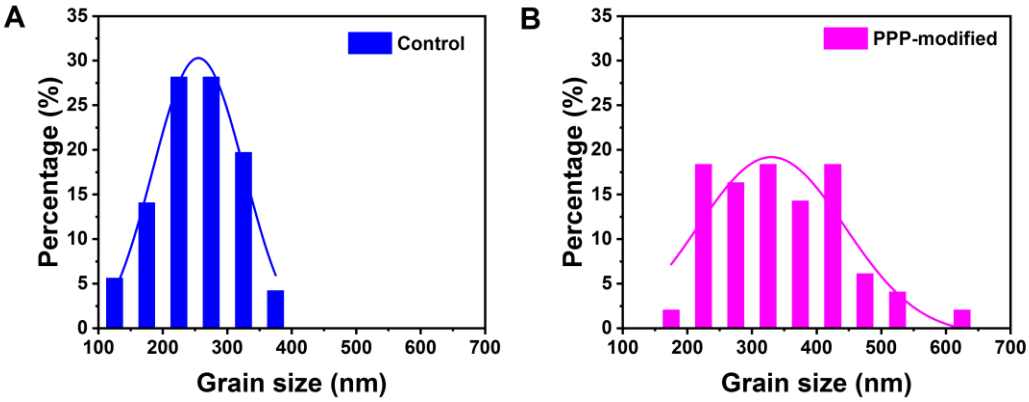

Fig. S6. Histogram of grain size distribution corresponding to the top-view SEM of the control and PPP-modified perovskite films.

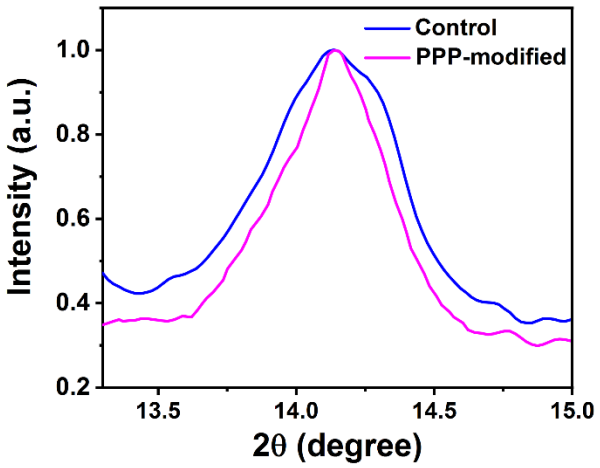

Fig. S7. The full width at half maximum (FWHM) of the (100) peak intensity area of the control and PPP-modified perovskite films.

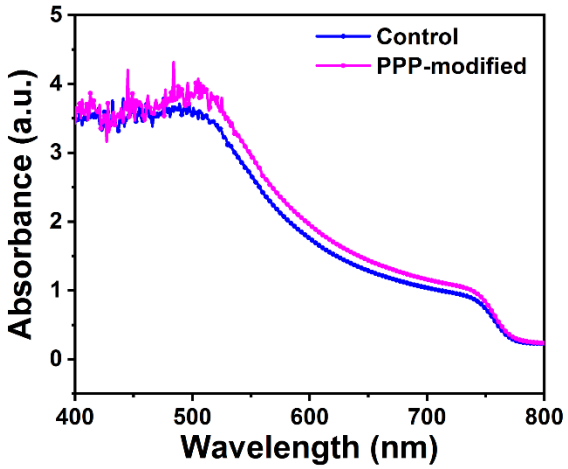

Fig. S8. UV-vis absorption spectra of the control and PPP-modified perovskite films.

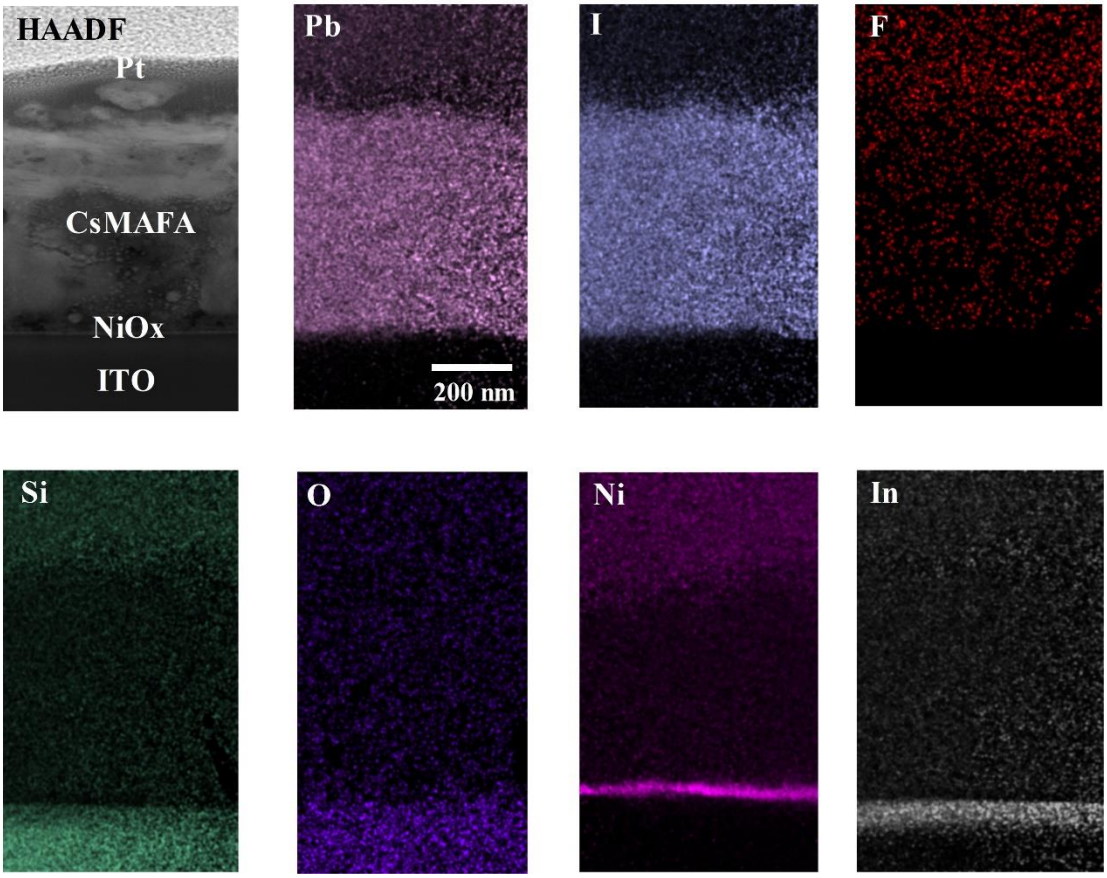

Fig. S9. Scanning transmission electron microscopy (STEM) images and the corresponding high-resolution EDX mapping of the lateral structure of the PPP-modified perovskite /NiOx /ITO.

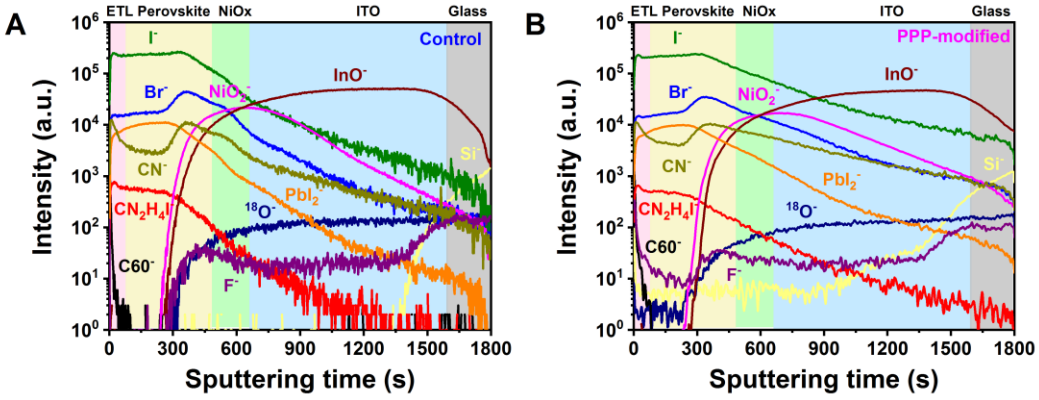

Fig. S10. The depth profiles of ToF-SIMS. Time of flight secondary-ion mass spectroscopy (ToF-SIMS) depth profiles of (A), control and (B), PPP-modified electrodeless PSC devices. $C60^-$ is selected for affirming the PCBM+C60 ETL, CN^- as representing the MA^+ and FA^+, $CN_2H_4I^-$ as representing the FAI, I^-, PbI_2^-, and Br^- for the CsMAFA perovskite. Note: at Fig. S10 A, NiO_2^- for the NiO_x, InO_2^- for the ITO, and Si^- for the glass; and at Fig. S10 B, $^{18}O^-$ and F^- for the PPP polymer, and Si^- for the PPP polymer and the glass.

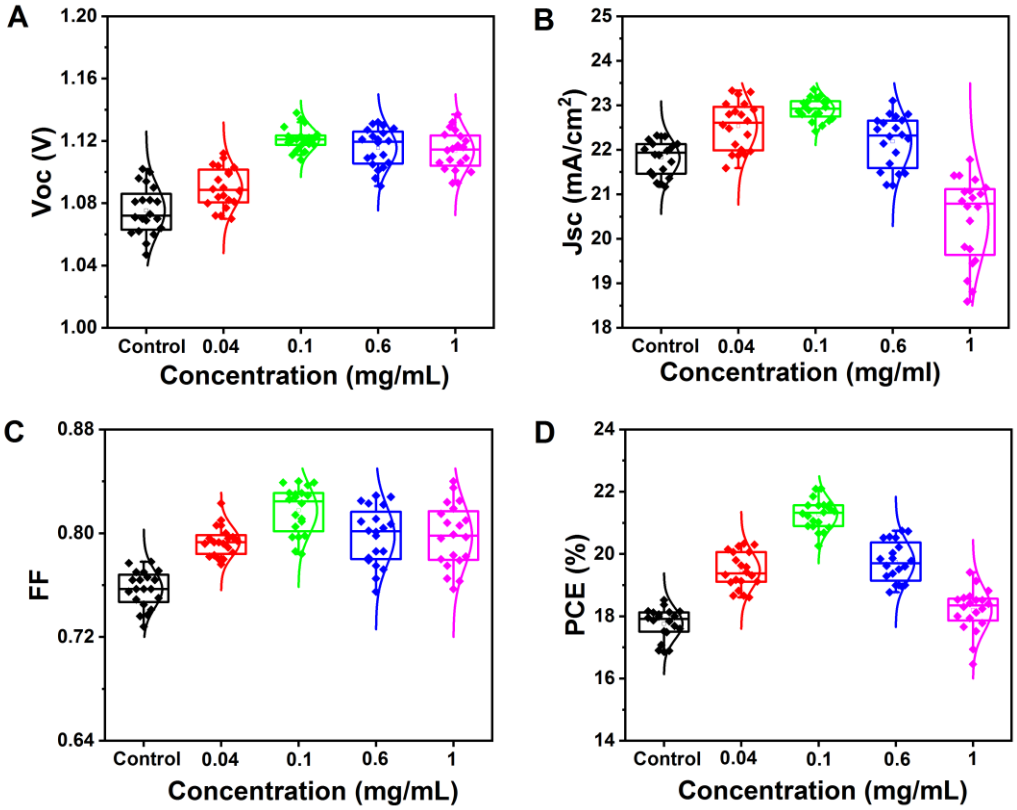

Fig. S11. Statistics of photovoltaic parameters. (**A**), V_{oc}, (**B**), J_{sc}, (**C**), FF, and (**D**), PCE statistics of 20 devices for the control PSCs and PPP-modified PSCs with different PPP concentration.

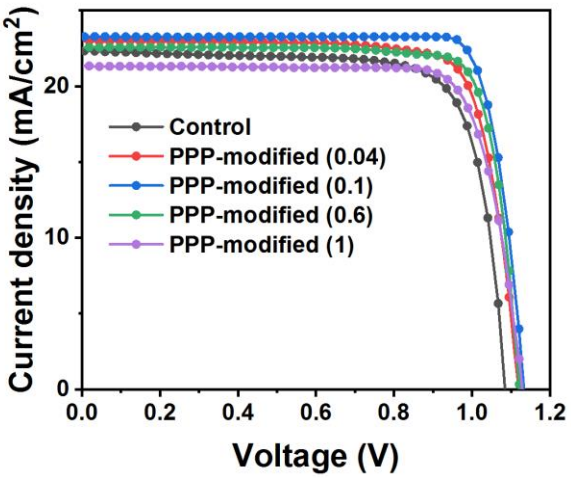

Fig. S12. Optimum *J*-*V* curves of the PSCs with different PPP polymer concentration (mg mL^{-1}) measured in the reverse scan direction.

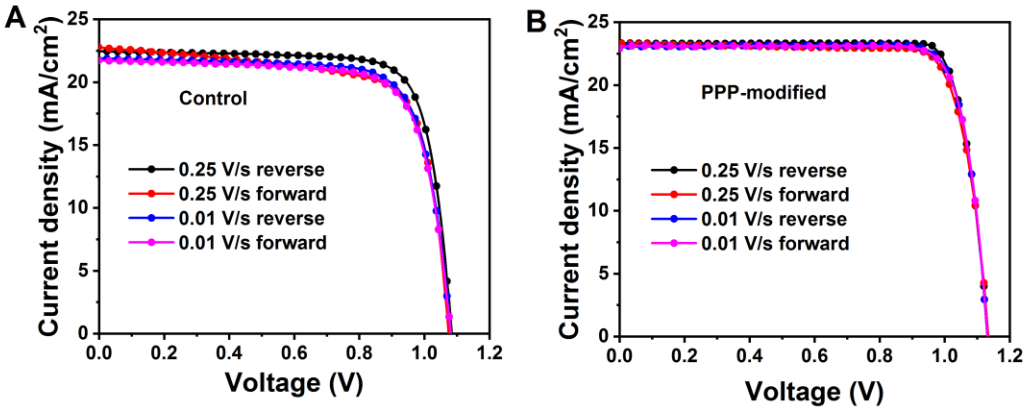

Fig. S13. The *J*-*V* curves of the champion devices of control and PPP-modified based on different sweep speed.

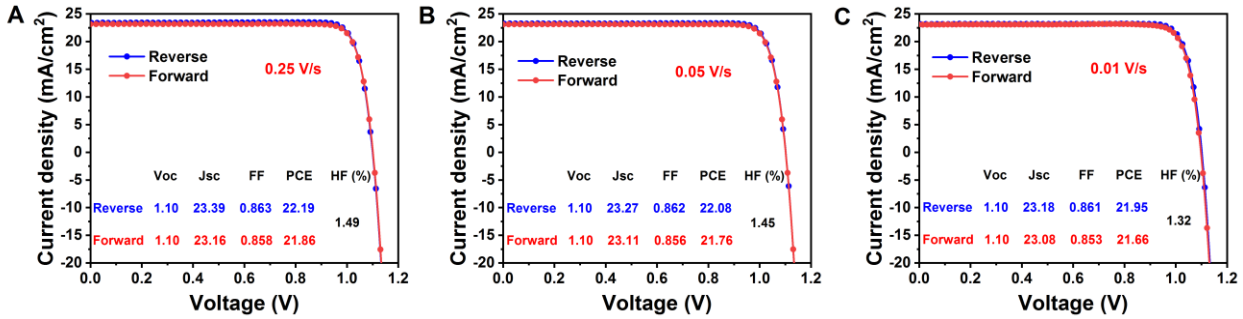

Fig. S14. *J*-*V* curves of the PPP-modified PSCs with the best FF based on different sweep speed. (**A**), 0.25 V s^{-1}, (**B**), 0.05 V s^{-1}, and (**C**), 0.01 V s^{-1}. HF represents hysteresis factor.

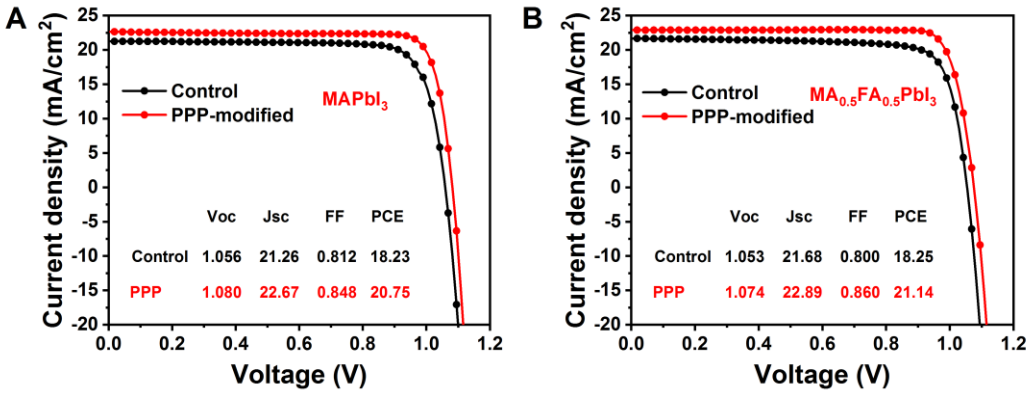

Fig. S15. The universality of PPP modification to improve device performance. *J-V* curves of the control and PPP-modified devices measured in the reverse scanning direction for different perovskite compositions: (**A**), $MAPbI_3$ and (**B**), $MA_{0.5}FA_{0.5}PbI_3$.

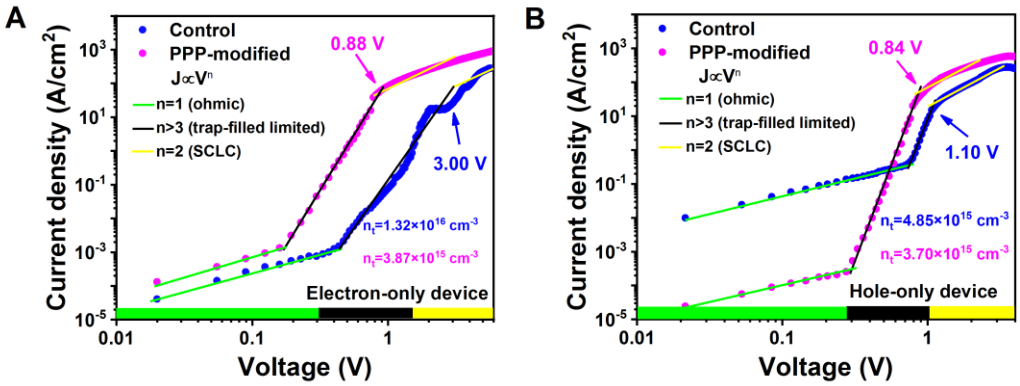

Fig. S16. Charge extraction characteristics analysis of PSCs. *J-V* curves of the (**A**), electron-only (ITO /SnO_2 /control or PPP-modified /PCBM /Ag) and (**B**), hole-only (ITO /NiOx /control or PPP-modified /spiro-MeOTAD /Au) devices.

The trap state density is derived from by trap-filled limiting voltage (V_{TFL}) using the equation:

$$V_{TFL} = \frac{en_tL^2}{2\varepsilon\varepsilon_0} \quad (1)$$

where e is the electron charge, n_t is trap state density, L is the thickness of perovskite film, ε is the relative dielectric constant of perovskite (ε=25.5), and ε_0 is the vacuum permittivity. V_{TFL} corresponds to the voltage at the intersection of the two *J-V* curves for the space charge limited and trap filling current regimes indicated by arrows Fig. S16.

The mobility is obtained according to the space charge limit current (SCLC) regions (n=2), the dark current is fitted by the Mott-Gurney law:

$$J = \frac{9}{8}\varepsilon\varepsilon_0\mu\frac{V^2}{L^3} \quad (2)$$

where J, μ, and V are the dark current density, the mobility of the control or the PPP-modified film, and applied voltage, respectively.

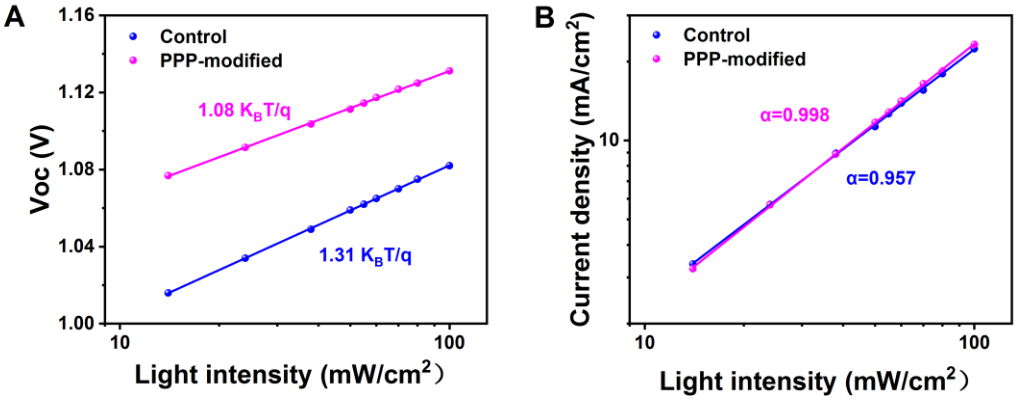

Fig. S17. Light intensity-dependent V_{oc} and J_{sc} for CsMAFA devices. (**A**), V_{oc} and (**B**), J_{sc} dependence on illumination intensity.

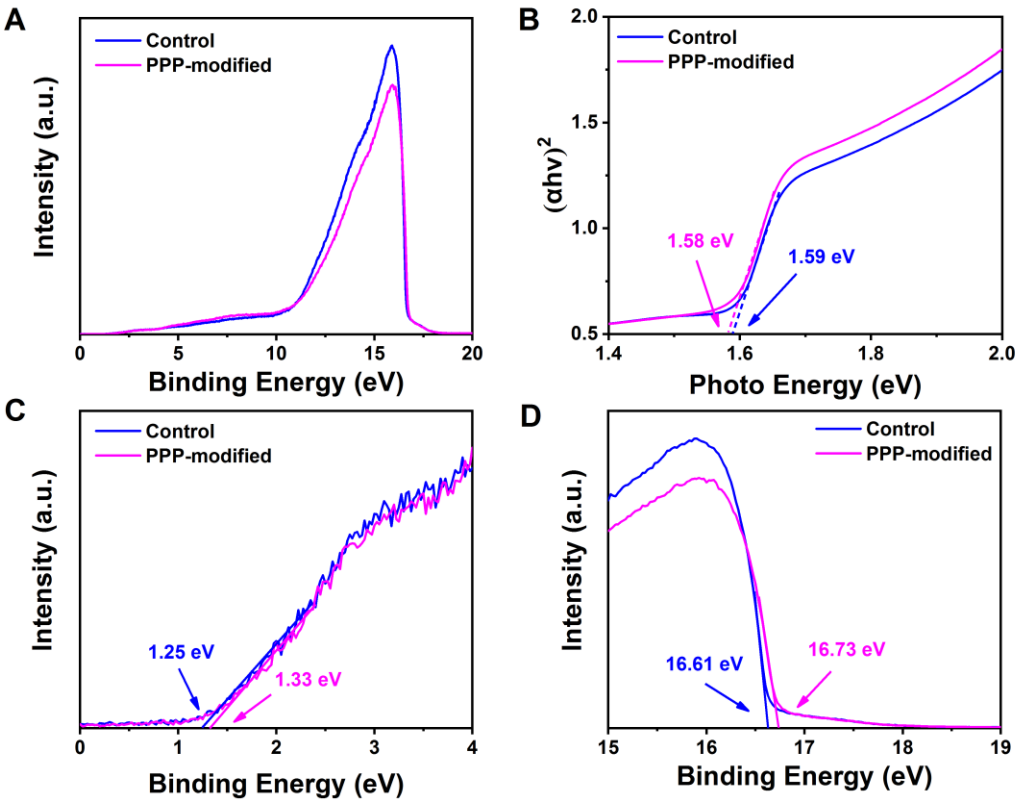

Fig. S18. Energy-level characterization of perovskite films. (**A**), UPS measurements of the control and PPP-modified films. (**B**), Tauc plots of the control and PPP-modified films. UPS spectra of the control and PPP-modified showing (**C**), the valence band region and (**D**), the secondary-electron cut-off (SECO) binding energy.

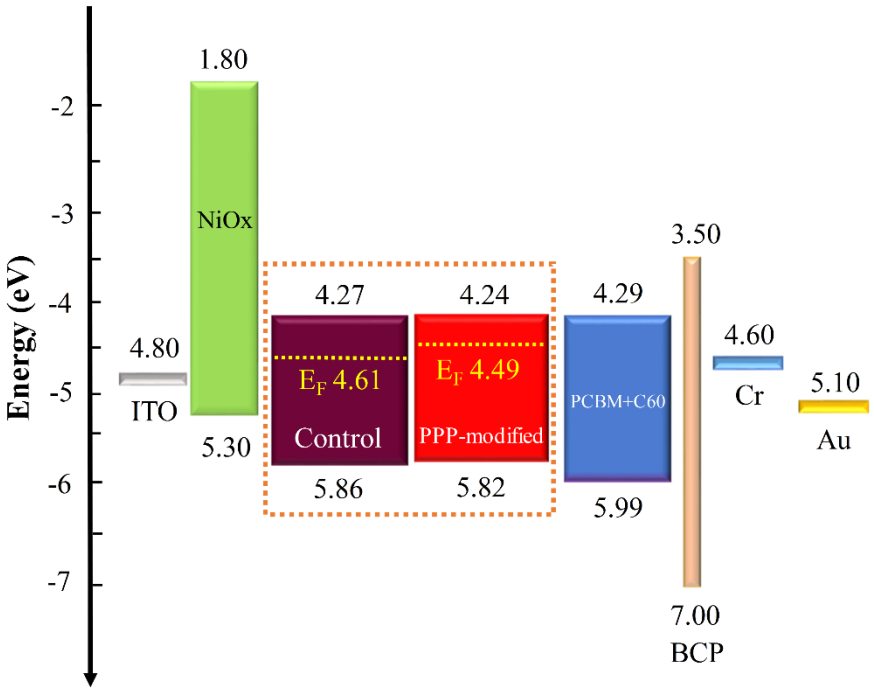

Fig. S19. The schematic energy level alignment of the solar cell.

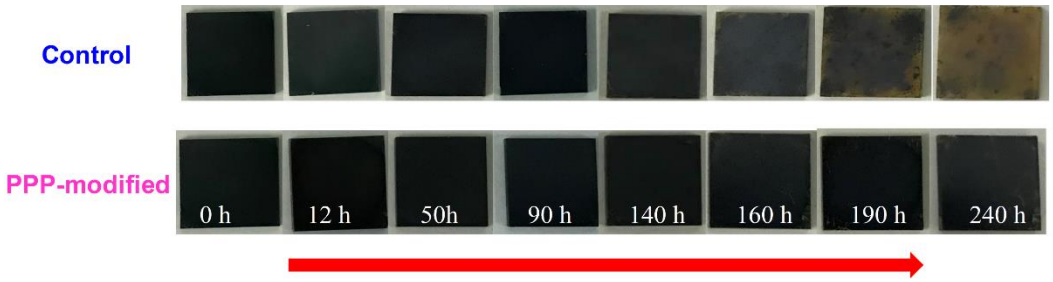

Fig. S20. The photographs of the control and PPP-modified perovskite films aging in air over time at 85 °C and 40% RH.

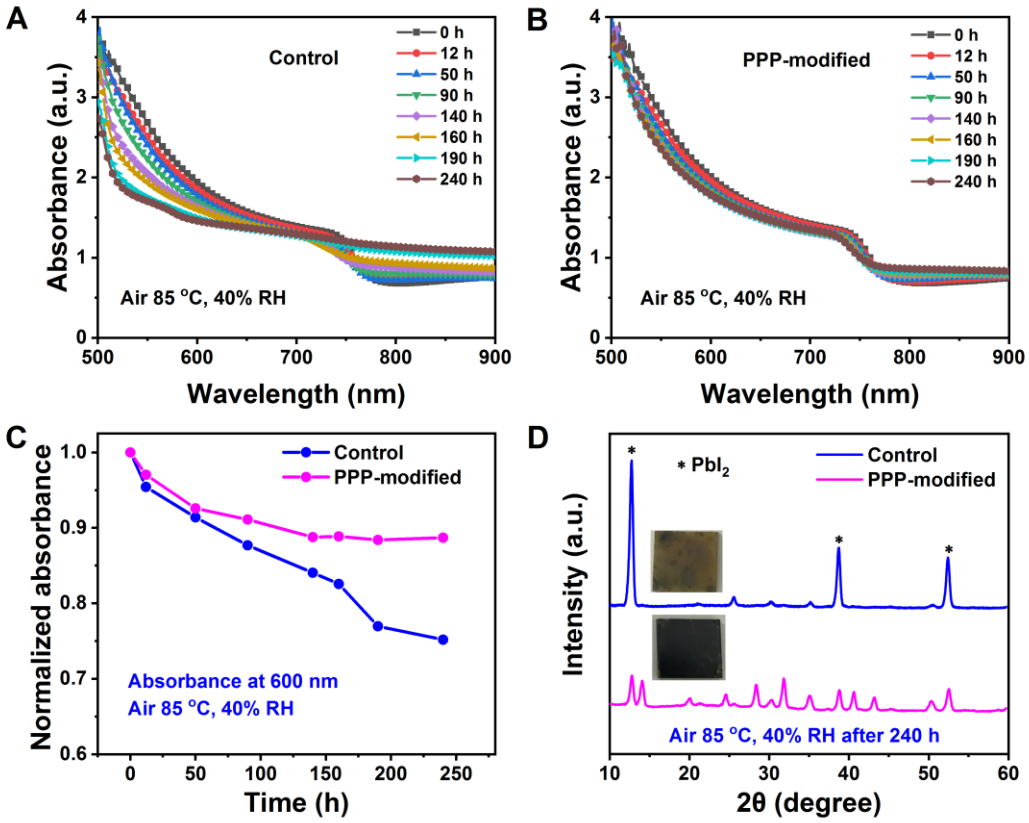

Fig. S21. Perovskite films degradation. (**A-B**), UV-vis absorption spectra and (**C**), the corresponding normalized UV-vis absorbance at 600 nm of the control and PPP-modified perovskite films as a function of aging time in air at 85 °C and 40% RH. (**D**), XRD patterns of the control and PPP-modified perovskite films after aged in air with 85 °C, 40% RH for 240 h.

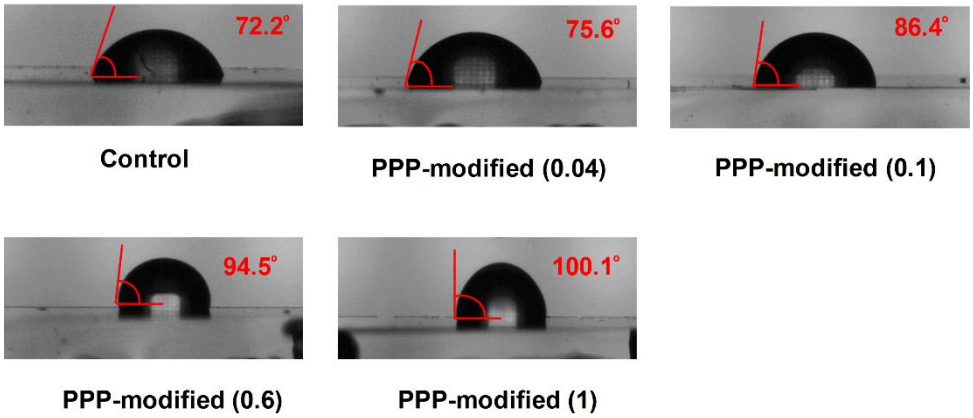

Fig. S22. The contact angle changes of the control and PPP-modified perovskite films with different PPP concentration (mg mL^{-1}).

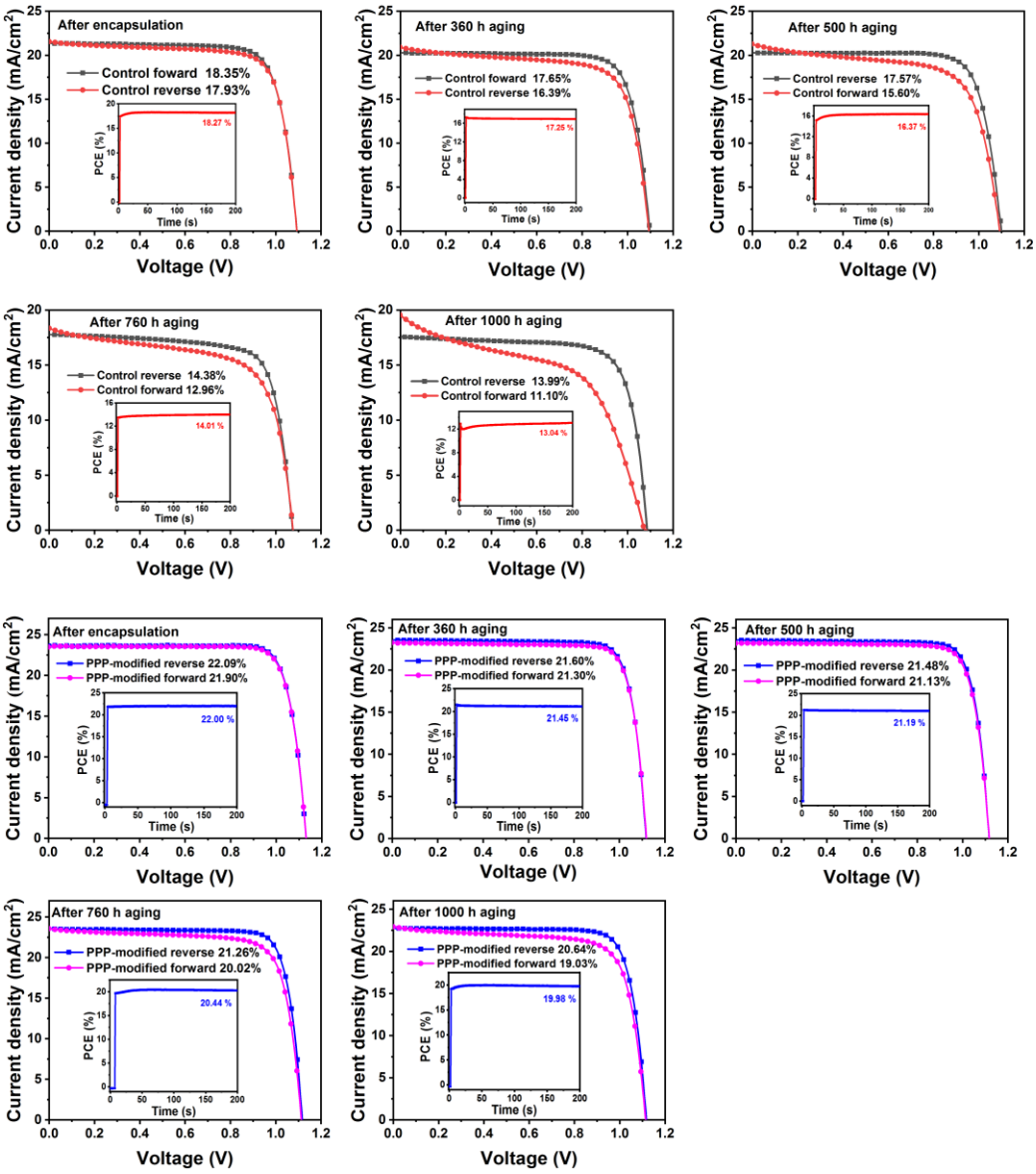

Fig. S23. Stability test. Most-stable device performance under combined full spectrum sunlight and heat stress for the control and PPP-modified PSCs.

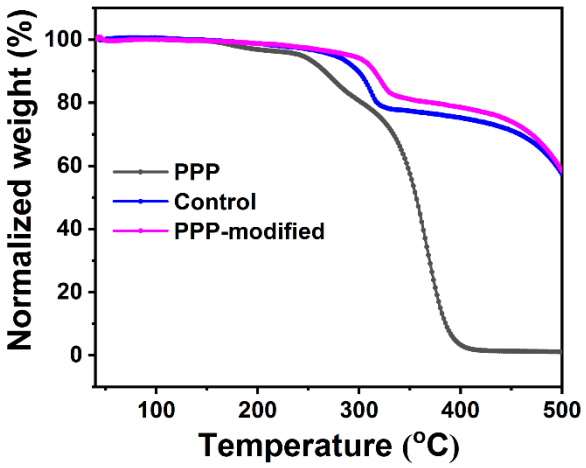

Fig. S24. Thermogravimetric analysis (TGA) curves of the PPP polymer, pristine perovskite, and PPP-modified perovskite.

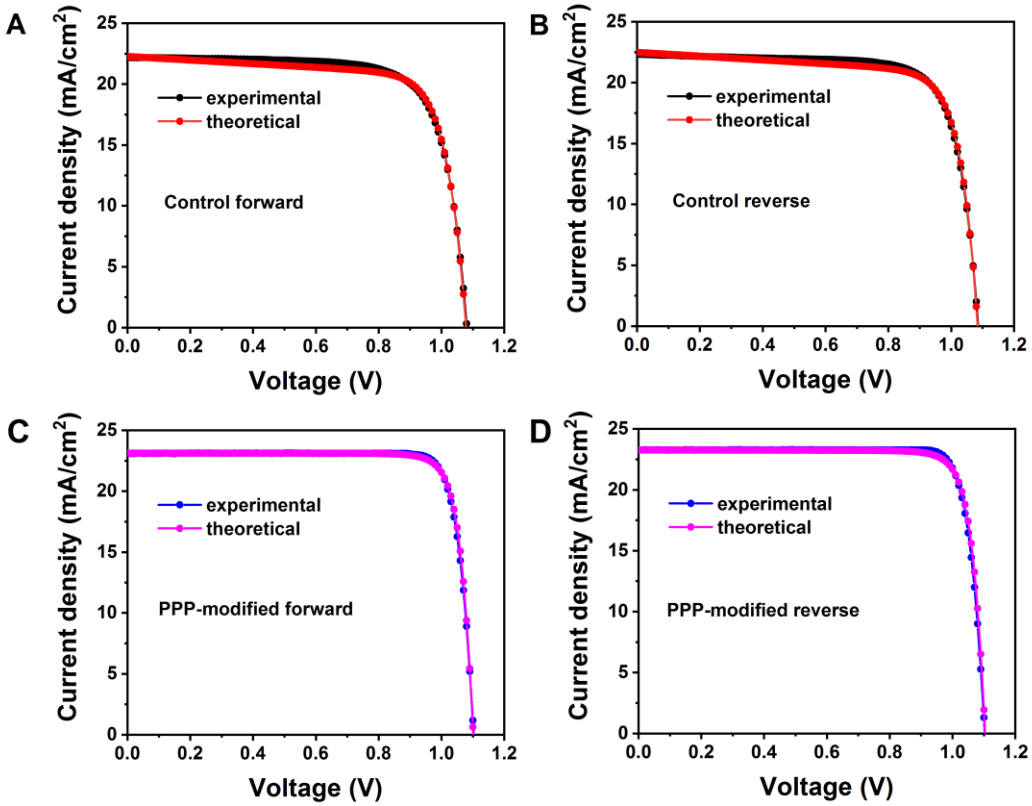

Fig. S25. The comparison of *J-V* curves between the theoretical simulation and experimental measurement. Theoretically fitted *J-V* curves by modified detailed balance model and experimentally measured *J-V* characteristics for (**A-B**), the control PSCs and (**C-D**), PPP-modified PSCs with the best FF.

In order to understand the loss mechanism and qualify loss proportions (loss factors) of FF, the revised detailed balance model is used

$$J = \frac{V-JR_S}{R_{sh}} + J_n(V - JR_s) + J_r(V - JR_s) - J_p \quad (3)$$

where V is the applied voltage, J_p is the photocurrent, J_r and J_n are the current loss due to the radiative emission and the nonradiative defect-induced recombination, respectively. R_s is the series resistance, which describes the ohmic loss by the contacts, carrier transport layers, and the hetero-junction interfaces between the perovskite and carrier transport layers. The defects, pinholes and voids induced current leakage is represented by the shunt resistance R_{sh}.

The photocurrent is given by

$$J_p = q\int_0^\infty \alpha(\lambda, L)\frac{\Gamma(\lambda)\lambda}{hc_0}d\lambda \quad (4)$$

where c_0 is the speed of light in air, Γ is the AM 1.5 G spectrum of Sun, λ is the wavelength and q is the elementary charge. The absorptivity α is the ratio of power absorbed by the perovskite active layer over the power of incident Sunlight. It can be obtained by numerically solving Maxwell equation. The refractive indices of materials can be obtained by ellipsometer measurement.

The radiative current is written as

$$J_r(V - JR_s) = J_0^r\left[exp\left(\frac{q(V-JR_S)}{k_BT}\right) - 1\right] \quad (5)$$

where k_B is the Boltzmann constant and T is the Kelvin temperature. Here, the radiative saturation current J_0^r is of the form

$$J_0^r = q\int_0^\infty \alpha(\lambda, L)\frac{\Gamma_0(\lambda)\lambda}{hc_0}d\lambda \quad (6)$$

It is proportional to the spectral overlap integral between the absorptivity α and black-body (thermal) emission spectrum Γ_0 at room temperature (T=300 K).

For perovskite solar cells, the dominant nonradiative recombination types are the bulk defect-induced recombination and the surface defect-induced recombination. Thus, the nonradiative current reads

$$J_n(V - JR_s) = qL\gamma_b n_i \, exp\left(\frac{q(V-JR_s)}{2k_BT}\right) + q\gamma_s \, exp\left(\frac{q(V-JR_s)}{k_BT}\right) \quad (7)$$

where γ_b and γ_s are the bulk nonradiative recombination rate and surface one, respectively, L is the perovskite active layer thickness, and n_i is the intrinsic carrier density of the perovskite material.

We will use the modified detailed balance model to fit the current density-voltage characteristics of the control and PPP-modified devices. The bulk nonradiative recombination rate γ_b, the surface nonradiative recombination rate γ_s, series resistance R_s, and shunt resistance R_{sh} will be retrieved. The ideal Shockley-Queisser (S-Q) limits of corresponding devices can be accessed by setting R_s =0, R_{sh} =∞, γ_b=0 and γ_s =0. Then, we can quantify the loss proportions of FF with the reference to its Shockley-Queisser limit. For example, the drop of FF solely by the bulk defect-induced recombination can be obtained by setting R_s =0, R_{sh} =∞ ,γ_s=0, but γ_b to its practical value (retrieved by the modified detailed balance model). Once we obtain the loss of FF values due to four factors, i.e. bulk defect-induced recombination, surface defect-induced recombination, R_s, and R_{sh}, we can obtain the weights or proportions of the four losses listed in Table S5. Table S5 lists the loss proportions (loss factors) of FF in the control and the PPP-modified devices, with reference to their S-Q limits achieved by setting R_s=0, R_{sh}=∞, γ_b=0 and γ_s=0. It can be seen that the loss proportions exhibit drastic reductions for the bulk defect-induced recombination and shunt resistance after incorporating the PPP polymer. Regarding the control device, with nearly 81% loss proportions, bulk defect-induced recombination contributes significantly to the low FF (0.770) with reference to its S-Q limit (0.904). After introducing the PPP material into active layer, the bulk defect-induced recombination and the shunt current are suppressed, and thus the FF is increased to 0.862 and with 30% loss proportions coming from the γ_b and near-zero form the R_{sh}. These findings confirm that the loss of FF (0.862) in the PPP-modified device with reference to its S-Q limit (0.904) is predominantly caused by the surface defect-induced recombination rather than by R_s and R_{sh}; and reduce the bulk defect-induced recombination can effectively enhance the FF.

Table S1. The best photovoltaic parameters of inverted PSCs for the control and PPP-modified device with different PPP concentration measured in reverse scan directions under standard AM 1.5 illumination (100 mW cm^{-2}). (Data in brackets are the average values of each parameter).

Concentration [mg mL^{-1}]	V_{oc} [V]	J_{sc} [mA cm^{-2}]	FF	PCE [%]
control (0)	1.082 (1.075±0.015)	22.32 (21.82±0.38)	0.770 (0.756±0.014)	18.62 (17.76±0.49)
0.04	1.119 (1.090±0.013)	22.97 (22.53±0.53)	0.792 (0.794±0.011)	20.36 (19.47±0.56)
0.1	1.131 (1.121±0.007)	23.24 (22.91±0.24)	0.841 (0.818±0.018)	22.11 (21.27±0.47)
0.6	1.121 (1.115±0.012)	22.56 (22.19±0.57)	0.822 (0.799±0.022)	20.79 (19.75±0.63)
1	1.128 (1.114±0.012)	21.32 (20.44±0.93)	0.796 (0.798±0.024)	19.14 (18.20±0.68)

Table S2. The champion photovoltaic parameters of inverted PSCs for the control and PPP-modified measured at different scanning speeds in different scanning directions under standard AM 1.5 illumination (100 mW cm^{-2}).

Device	Direction	Speed [V s^{-1}]	V_{oc} [V]	J_{sc} [mA cm^{-2}]	FF	PCE [%]	Hysteresis Factor [%]
control	reverse	0.25	1.083	22.45	0.783	18.76	5.81
	forward		1.074	22.77	0.722	17.67	
	reverse	0.01	1.081	21.88	0.757	17.91	1.84
	forward		1.080	21.72	0.749	17.58	
PPP-modified	reverse	0.25	1.131	23.30	0.841	22.15	1.02
	forward		1.131	23.16	0.837	21.92	
	reverse	0.01	1.131	23.22	0.840	22.05	0.88
	forward		1.131	23.10	0.837	21.87	

Table S3. The comparison of FF and PCE for the previous studies based on the modification of interfacial and active layer.

Materials/ Methods	Device structure	V_{oc} [V]	J_{sc} [mA cm^{-2}]	FF	PCE [%]	Year/Ref.
$A_{10}C_{60}$	ITO/PEDOT:PSS/$MAPbI_3$:$A_{10}C_{60}$/$PC_{61}BM$/Al	0.86	18.1	0.867	13.5	2015 *(40)*
H_2O	ITO/PEDOT:PSS/$MAPbI_3$/$PC_{71}BM$/Ca/Al	1.03	20.6	0.850	18.0	2015 *(41)*
$BMIMBF_4$	FTO/NiOx/ $(FA_{0.83}MA_{0.17})_{0.95}Cs_{0.05}Pb(I_{0.9}Br_{0.1})_3$-$BMIMBF_4$/PCBM/BCP/$Cr(Cr_2O_3)$/Au	1.08	23.8	0.810	19.8	2019 *(24)*
PBTI	ITO/NiOx/CsFAMA-PBTI/PCBM/ZrAcac/Ag	1.13	22.9	0.795	20.6	2019 *(49)*
PMMA	ITO/PTAA/PMMA/ $Cs_{0.05}(FA_{0.85}MA_{0.15})_{0.95}Pb(I_{0.85}Br_{0.15})_3$/C60/BCP/Ag	1.12	23.1	0.803	20.8	2019 *(50)*
ASE-GB-H_2O	ITO/PEDOT:PSS/$MAPbI_3$/C60/BCP/Ag	1.06	23.1	0.860	21.0	2018 *(42)*
$C_8H_{17}NH_3)_2SO_4$	ITO/PTAA/$Cs_{0.05}FA_{0.81}MA_{0.14}PbI_{2.55}Br_{0.45}$ - $C_8H_{17}NH_3)_2SO_4$/C60/BCP/Cu	1.16	22.6	0.804	21.1	2019 *(45)*
Oligomeric Silica (OS)	ITO/PTAA/$FA_{0.85}MA_{0.15}Pb(I_{0.85}Br_{0.15})_3$@OS/PCBM/C60/BCP/Cu	1.15	23.1	0.811	21.5	2019 *(43)*
DMAI	ITO/NiO_x/$MA_{0.89}DMA_{0.11}PbI_3$/choline chloride/C60/BCP/Ag	1.12	23.5	0.820	21.6	2019 *(44)*
LAIs	ITO/PTAA-LAIs/$(CsPbI_3)_{0.05}$($FA_{0.85}MA_{0.15}Pb(I_{0.85}Br_{0.15})_3)_{0.95}$ /PCBM/BCP/Ag	1.21	22.6	0.816	22.3	2020 *(48)*
F2TCNQ	ITO/NiOx/F2TCNQ/ $(CsPbI_3)_{0.05}[(FAPbI_3)_{0.85}(MAPbBr_3)_{0.15}]_{0.95}$ /PCBM/BCP/Ag	1.15	23.6	0.830	22.5	2020 *(46)*
AALs	ITO/PTAA/$Cs_{0.05}(FA_{0.92}MA_{0.08})_{0.95}$ $Pb(I_{0.92}$. $Br_{0.08})_3$-AALs/C60/BCP/Cu	1.17	24.1	0.816	23.0	2020 *(8)*
room-temperature (RT) crystallizing	ITO/NiOx/RT-$MAPb(I_{1-x}Cl_x)_3$/PCBM/BCP/Ag	1.16	23.52	0.847	23.1	2020 *(47)*
PPP	ITO/NiOx/$Cs_{0.05}(FA_{0.85}MA_{0.15})_{0.95}Pb(I_{0.85}Br_{0.15}$ $)_3$-PPP/PCBM+C60/BCP/Cr/Au	1.13 1.10	23.2 23.3	0.841 0.862	22.1 22.1	This work

Table S4. Comparison of the stability of the solar cells in our work with some recent reports. PCE_0 and PCE_t are the efficiency of devices before and after stability tests.

Device structure	Light source	Ageing condition	Degradation factor	PCE_0 [%]	PCE_t/PCE_0	Reference
Planar n-i-p structure						
ITO/TiO_2-Cl/perovskite/Spiro-OMeTAD/Au	Xenon lamp*	Nitrogen, SPO,500 h	Light (without UV)	~20	90%	Science, 2017 *(61)*
ITO/C60-SAM/SnO_x/PCBM/perovskite /polymer/Ta-WO_x/Au	White LED	Nitrogen, Open-circuit,1000 h	Light (without UV)	~20	95%	Science, 2017 *(62)*
ITO/SnO_2/perovskite/ EH44/MoOx/Al	Plasma lamp	Air, RH ~10-20% SPO,1000 h	Light (with UV), 20-30 °C	~12%	94%	Nat. Energy, 2018 *(63)*
ITO/SnO_2/PCBM:PMMA/ perovskite/PMMA/HTM /Au	White LED	Nitrogen, SPO,1000 h	Light (without UV), 20 °C	19.54	78%	Science, 2018 *(64)*
ITO/d-TiO_2/ mp-TiO_2/ perovskite/WBH/P3HT/ Au	White LED	Air, RH ~30%, encapsulated, SPO, 1370 h	Light (without UV), 25 °C	N.A	95%	Nature, 2019 *(11)*
Planar p-i-n structure						
FTO/LiMgNiO/perovskite/ PCBM/Nb-TiO_2/Ag	Xenon lamp*	Dry cabinet, RH <20%, encapsulated, SPO,1000h	Light (without UV), 45-50 °C	~16	>90%	Science, 2015 *(65)*
ITO/NiOx/perovskite /PCBM/ZrAcac/Ag	Xenon lamp	Air, RH ~35%, encapsulated, SPO, 200 h	Light (with UV), ~23 °C	N.A	76%	Adv. Funct. Mater. 2019 *(49)*
ITO/SM-HTMs /perovskite/C60/BCP/Ag	White LED	Air, RH ~34%, encapsulated, SPO, 500 h	Light (without UV), 25 °C	N.A	90%	Adv. Mater. 2019 *(66)*
ITO/NiO_x/perovskite /choline chloride/C60/BCP/Ag	White LED	Air, RH ~25%, encapsulated, SPO, 800 h	Light (without UV), 20 °C	18	80%	Adv. Mater. 2019 *(44)*
ITO/PTAA/perovskite /C60/BCP/Cu	Plasma lamp	Air, RH ~60, SPO,1200 h	Light (with UV), 65 °C	19.44	96.8 %	Science, 2019 *(45)*
ITO/PTAA- BDAI/perovskite /PCBM/BCP/Ag	White LED	N_2, SPO,10 h	Light (without UV), 25 °C	~21.8	98.6 %	Joule 2020 *(48)*
ITO/PTAA/perovskite-AALs/C60/BCP/Cu	Xenon lamp*	N_2, encapsulated, SPO, 1000 h	Light (without UV), 40 °C	21.2	No loss	Nat. Energy 2020 *(8)*
ITO/NiOx/perovskite-PPP/PCBM+C60/BCP/Cr/Au	**Xenon lamp**	**Air, RH ~40%, encapsulated, open-circuit,1000 h**	**Light (with UV), ~75 °C**	**22.0**	**91%**	**This work**
	White LED	**Air, RH ~40%, encapsulated, SPO, 1000 h**	**Light (with UV), ~45 °C**	**~21**	**No loss**	

*A 420-nm cutoff UV filter was used during this stability test.

Table S5. Loss proportions of FF (with reference to their Shockley-Queisser limits) for the control and PPP-modified devices. F and R represent forward and reverse scanning modes.

Loss proportions	Bulk defect-induced recombination	Surface defect-induced recombination	Series resistance	Shunt resistance
Control (F)	82.64%	2.15%	6.61%	8.60%
Control (R)	80.97%	4.46%	4.23%	10.34%
PPP-modified (F)	29.18%	62.83%	7.91%	0.08%
PPP-modified (R)	33.06%	58.10%	8.48%	0.36%

Data S1. (separate file)

The source data for supporting the conclusions in this manuscript.

REFERENCES AND NOTES

1. X. Li, F. Zhang, H. He, J. J. Berry, K. Zhu, T. Xu, On-device lead sequestration for perovskite solar cells. *Nature* **578**, 555–558 (2020).

2. M. Yang, Z. Li, M. O. Reese, O. G. Reid, D. H. Kim, S. Siol, T. R. Klein, Y. Yan, J. J. Berry, M. F. A. M. van Hest, K. Zhu, Perovskite ink with wide processing window for scalable high-efficiency solar cells. *Nat. Energy* **2**, 17038 (2017).

3. J. Burschka, N. Pellet, S. J. Moon, R. Humphry-Baker, P. Gao, M. K. Nazeeruddin, M. Grätzel, Sequential deposition as a route to high-performance perovskite-sensitized solar cells. *Nature* **499**, 316–319 (2013).

4. Q. Dong, Y. Fang, Y. Shao, P. Mulligan, J. Qiu, L. Cao, J. Huang, Electron-hole diffusion lengths > 175 μm in solution-grown $CH_3NH_3PbI_3$ single crystals. *Science* **347**, 967–970 (2015).

5. T. Niu, J. Lu, R. Munir, J. Li, D. Barrit, X. Zhang, H. Hu, Z. Yang, A. Amassian, K. Zhao, S. F. Liu, Stable high-performance perovskite solar cells via grain boundary passivation. *Adv. Mater.* **30**, 1706576 (2018).

6. Best Research Cell Efficiency Records, *Nation Renewable Energy Laboratory (NREL)* (2021); www.nrel.gov/pv/cell-efficiency.html.

7. J. J. Yoo, G. Seo, M. R. Chua, T. G. Park, Y. Lu, F. Rotermund, Y.-K. Kim, C. S. Moon, N. J. Jeon, J.-P. Correa-Baena, V. Bulović, S. S. Shin, M. G. Bawendi, J. Seo, Efficient perovskite solar cells via improved carrier management. *Nature* **590**, 587–593 (2021).

8. X. Zheng, Y. Hou, C. Bao, J. Yin, F. Yuan, Z. Huang, K. Song, J. Liu, J. Troughton, N. Gasparini, C. Zhou, Y. Lin, D.-J. Xue, B. Chen, A. K. Johnston, N. Wei, M. N. Hedhili, M. Wei, A. Y. Alsalloum, P. Maity, B. Turedi, C. Yang, D. Baran, T. D. Anthopoulos, Y. Han, Z.-H. Lu, O. F. Mohammed, F. Gao, E. H. Sargent, O. M. Bakr, Managing grains and interfaces via ligand anchoring enables 22.3%-efficiency inverted perovskite solar cells. *Nat. Energy* **5**, 131–140 (2020).

9. H. Min, M. Kim, S.-U. Lee, H. Kim, G. Kim, K. Choi, J. H. Lee, S. I. Seok, Efficient, stable solar cells by using inherent bandgap of α-phase formamidinium lead iodide. *Science* **366**, 749–753 (2019).

10. P. Schulz, D. Cahen, A. Kahn, Halide perovskites: Is it all about the interfaces? *Chem. Rev.* **119**, 3349–3417 (2019).

11. E. H. Jung, N. J. Jeon, E. Y. Park, C. S. Moon, T. J. Shin, T.-Y. Yang, J. H. Noh, J. Seo, Efficient, stable and scalable perovskite solar cells using poly(3-hexylthiophene). *Nature* **567**, 511–515 (2019).

12. Q. Jiang, Y. Zhao, X. Zhang, X. Yang, Y. Chen, Z. Chu, Q. Ye, X. Li, Z. Yin, J. You, Surface passivation of perovskite film for efficient solar cells. *Nat. Photonics* **13**, 460–466 (2019).

13. B. Qi, J. Wang, Fill factor in organic solar cells. *Phys. Chem. Chem. Phys.* **15**, 8972–8982 (2013).

14. N. Mundhaas, Z. J. Yu, K. A. Bush, H.-P. Wang, J. Häusele, S. Kavadiya, M. D. McGehee, Z. C. Holman, Series resistance measurements of perovskite solar cells using J_{sc}–V_{oc} measurements. *Sol. RRL* **3**, 1800378 (2019).

15. H. D. Kim, H. Ohkita, Potential improvement in fill factor of lead-halide perovskite solar cells. *Sol. RRL* **1**, 1700027 (2017).

16. D. Luo, R. Su, W. Zhang, Q. Gong, R. Zhu, Minimizing non-radiative recombination losses in perovskite solar cells. *Nat. Rev. Mater.* **5**, 44–60 (2020).

17. H. Zhang, M. K. Nazeeruddin, W. C. H. Choy, Perovskite photovoltaics: The significant role of ligands in film formation, passivation, and stability. *Adv. Mater.* **31**, 1805702 (2019).

18. Y. Bai, X. Meng, S. Yang, Interface engineering for highly efficient and stable planar p-i-n perovskite solar cells. *Adv. Energy Mater.* **8**, 1701883 (2018).

19. F. Gao, Y. Zhao, X. Zhang, J. You, Recent progresses on defect passivation toward efficient perovskite solar cells. *Adv. Energy Mater.* **10**, 1902650 (2020).

20. S. Liu, Y. Guan, Y. Sheng, Y. Hu, Y. Rong, A. Mei, H. Han, A review on additives for halide perovskite solar cells. *Adv. Energy Mater.* **10**, 1902492 (2020).

21. F. Zhang, K. Zhu, Additive engineering for efficient and stable perovskite solar cells. *Adv. Energy Mater.* **10**, 1902579 (2020).

22. J. W. Lee, Z. Dai, C. Lee, H. M. Lee, T. H. Han, N. De Marco, O. Lin, C. S. Choi, B. Dunn, J. Koh, D. Di Carlo, J. H. Ko, H. D. Maynard, Y. Yang, Tuning molecular interactions for highly reproducible and efficient formamidinium perovskite solar cells via adduct approach. *J. Am. Chem. Soc.* **140**, 6317–6324 (2018).

23. Y.-H. Lin, N. Sakai, P. Da, J. Wu, H. C. Sansom, A. J. Ramadan, S. Mahesh, J. Liu, R. D. J. Oliver, J. Lim, L. Aspitarte, K. Sharma, P. K. Madhu, A. B. Morales-Vilches, P. K. Nayak, S. Bai, F. Gao, C. R. M. Grovenor, M. B. Johnston, J. G. Labram, J. R. Durrant, J. M. Ball, B. Wenger, B. Stannowski, H. J. Snaith, A piperidinium salt stabilizes efficient metal-halide perovskite solar cells. *Science* **369**, 96–102 (2020).

24. S. Bai, P. Da, C. Li, Z. Wang, Z. Yuan, F. Fu, M. Kawecki, X. Liu, N. Sakai, J. T.-W. Wang, S. Huettner, S. Buecheler, M. Fahlman, F. Gao, H. J. Snaith, Planar perovskite solar cells with long-term stability using ionic liquid additives. *Nature* **571**, 245–250 (2019).

25. N. K. Noel, A. Abate, S. D. Stranks, E. S. Parrott, V. M. Burlakov, A. Goriely, H. J. Snaith, Enhanced photoluminescence and solar cell performance via lewis base passivation of organic–inorganic lead halide perovskites. *ACS Nano* **8**, 9815–9821 (2014).

26. R. Wang, J. Xue, L. Meng, J.-W. Lee, Z. Zhao, P. Sun, L. Cai, T. Huang, Z. Wang, Z.-K. Wang, Y. Duan, J. L. Yang, S. Tan, Y. Yuan, Y. Huang, Y. Yang, Caffeine improves the performance and thermal stability of perovskite solar cells. *Joule* **3**, 1464–1477 (2019).

27. C.-H. Chiang, C.-G. Wu, Bulk heterojunction perovskite-PCBM solar cells with high fill factor. *Nat. Photonics* **10**, 196–200 (2016).

28. D. Bi, C. Yi, J. Luo, J.-D. Décoppet, F. Zhang, S. M. Zakeeruddin, X. Li, A. Hagfeldt, M. Grätzel, Polymer-templated nucleation and crystal growth of perovskite films for solar cells with efficiency greater than 21%. *Nat. Energy* **1**, 16142 (2016).

29. T. H. Han, J. W. Lee, C. Choi, S. Tan, C. Lee, Y. Zhao, Z. Dai, N. De Marco, S. J. Lee, S. H. Bae, Y. Yuan, H. M. Lee, Y. Huang, Y. Yang, Perovskite-polymer composite cross-linker approach for highly-stable and efficient perovskite solar cells. *Nat. Commun.* **10**, 520 (2019).

30. T. Elmelund, B. Seger, M. Kuno, P. V. Kamat, How interplay between photo and thermal activation dictates halide ion segregation in mixed halide perovskites. *ACS Energy Lett.* **5**, 56–63 (2020).

31. J. S. Yun, J. Kim, T. Young, R. J. Patterson, D. Kim, J. Seidel, S. Lim, M. A. Green, S. Huang, A. Ho-Baillie, Humidity-induced degradation via grain boundaries of $HC(NH_2)_2PbI_3$ planar perovskite solar cells. *Adv. Funct. Mater.* **28**, 1705363 (2018).

32. Y. Jiang, S.-C. Yang, Q. Jeangros, S. Pisoni, T. Moser, S. Buecheler, A. N. Tiwari, F. Fu, Mitigation of vacuum and illumination-induced degradation in perovskite solar cells by structure engineering. *Joule* **4**, 1087–1103 (2020).

33. N. Li, Y. Luo, Z. Chen, X. Niu, X. Zhang, J. Lu, R. Kumar, J. Jiang, H. Liu, X. Guo, B. Lai, G. Brocks, Q. Chen, S. Tao, D. P. Fenning, H. Zhou, Microscopic degradation in formamidinium-cesium lead iodide perovskite solar cells under operational stressors. *Joule* **4**, 1743–1758 (2020).

34. Y. Zhao, J. Wei, H. Li, Y. Yan, W. Zhou, D. Yu, Q. Zhao, A polymer scaffold for self-healing perovskite solar cells. *Nat. Commun.* **7**, 10228 (2016).

35. W. Zhang, G. Camino, R. Yang, Polymer/polyhedral oligomeric silsesquioxane (POSS) nanocomposites: An overview of fire retardance. *Prog. Polym. Sci.* **67**, 77–125 (2017).

36. S. Valero, T. Soria, N. Marinova, J. L. Delgado, Efficient and stable perovskite solar cells based on perfluorinated polymers. *Polym. Chem.* **10**, 5726–5736 (2019).

37. L. Meng, C. Sun, R. Wang, W. Huang, Z. Zhao, P. Sun, T. Huang, J. Xue, J. W. Lee, C. Zhu, Y. Huang, Y. Li, Y. Yang, Tailored phase conversion under conjugated polymer enables thermally stable perovskite solar cells with efficiency exceeding 21%. *J. Am. Chem. Soc.* **140**, 17255–17262 (2018).

38. C.-C. Zhang, Z.-K. Wang, S. Yuan, R. Wang, M. Li, M. F. Jimoh, L.-S. Liao, Y. Yang, Polarized ferroelectric polymers for high-performance perovskite solar cells. *Adv. Mater.* **31**, 1902222 (2019).

39. S. Rühle, Tabulated values of the Shockley-Queisser limit for single junction solar cells. *Sol. Energy* **130**, 139–147 (2016).

40. K. Wang, C. Liu, P. Du, J. Zheng, X. Gong, Bulk heterojunction perovskite hybrid solar cells with large fill factor. *Energ. Environ. Sci.* **8**, 1245–1255 (2015).

41. C.-G. Wu, C.-H. Chiang, Z.-L. Tseng, M. K. Nazeeruddin, A. Hagfeldt, M. Grätzel, High efficiency stable inverted perovskite solar cells without current hysteresis. *Energ. Environ. Sci.* **8**, 2725–2733 (2015).

42. C. H. Chiang, C. G. Wu, A method for the preparation of highly oriented $MAPbI_3$ crystallites for high-efficiency perovskite solar cells to achieve an 86% fill factor. *ACS Nano* **12**, 10355–10364 (2018).

43. Y. Bai, Y. Lin, L. Ren, X. Shi, E. Strounina, Y. Deng, Q. Wang, Y. Fang, X. Zheng, Y. Lin, Z.-G. Chen, Y. Du, L. Wang, J. Huang, Oligomeric silica-wrapped perovskites enable synchronous defect passivation and grain stabilization for efficient and stable perovskite photovoltaics. *ACS Energy Lett.* **4**, 1231–1240 (2019).

44. H. Chen, Q. Wei, M. I. Saidaminov, F. Wang, A. Johnston, Y. Hou, Z. Peng, K. Xu, W. Zhou, Z. Liu, L. Qiao, X. Wang, S. Xu, J. Li, R. Long, Y. Ke, E. H. Sargent, Z. Ning, Efficient and stable inverted perovskite solar cells incorporating secondary amines. *Adv. Mater.* **31**, 1903559 (2019).

45. S. Yang , S. Chen , E. Mosconi, Y. Fang, X. Xiao, C. Wang, Y. Zhou , Z. Yu, J. Zhao, Y. Gao, F. De Angelis, J. Huang, Stabilizing halide perovskite surfaces for solar cell operation with wide-bandgap lead oxysalts. *Science* **365**, 473–478 (2019).

46. P. Ru, E. Bi, Y. Zhang, Y. Wang, W. Kong, Y. Sha, W. Tang, P. Zhang, Y. Wu, W. Chen, X. Yang, H. Chen, L. Han, High electron affinity enables fast hole extraction for efficient flexible inverted perovskite solar cells. *Adv. Energy Mater.* **10**, 1903487 (2020).

47. K. Wang, C. Wu, Y. Hou, D. Yang, T. Ye, J. Yoon, M. Sanghadasa, S. Priya, Isothermally crystallized perovskites at room-temperature. *Energ. Environ. Sci.***13**, 3412–3422 (2020).

48. S. Wu, J. Zhang, Z. Li, D. Liu, M. Qin, S. H. Cheung, X. Lu, D. Lei, S. K. So, Z. Zhu, A. K. Y. Jen, Modulation of defects and interfaces through alkylammonium interlayer for efficient inverted perovskite solar cells. *Joule* **4**, 1248–1262 (2020).

49. W. Chen, Y. Wang, G. Pang, C. W. Koh, A. B. Djurišić, Y. Wu, B. Tu, F.-z. Liu, R. Chen, H. Y. Woo, X. Guo, Z. He, Conjugated polymer-assisted grain boundary passivation for efficient inverted planar perovskite solar cells. *Adv. Funct. Mater.* **29**, 1808855 (2019).

50. X. Liu, Y. Cheng, C. Liu, T. Zhang, N. Zhang, S. Zhang, J. Chen, Q. Xu, 20.7% highly reproducible inverted planar perovskite solar cells with enhanced fill factor and eliminated hysteresis. *Energ. Environ. Sci.* **12**, 1622–1633 (2019).

51. T. S. Su, F. T. Eickemeyer, M. A. Hope, F. Jahanbakhshi, M. Mladenovic, J. Li, Z. Zhou, A. Mishra, J. H. Yum, D. Ren, A. Krishna, O. Ouellette, T. C. Wei, H. Zhou, H. H. Huang, M. D. Mensi, K. Sivula, S. M. Zakeeruddin, J. V. Milic, A. Hagfeldt, U. Rothlisberger, L. Emsley, H. Zhang, M. Gratzel, Crown ether modulation enables over 23% efficient formamidinium-based perovskite solar cells. *J. Am. Chem. Soc.* **142**, 19980–19991 (2020).

52. M. A. Green, Accuracy of analytical expressions for solar cell fill factors. *Sol. Cells* **7**, 337–340 (1982).

53. J. Wang, J. Zhang, Y. Zhou, H. Liu, Q. Xue, X. Li, C.-C. Chueh, H.-L. Yip, Z. Zhu, A. K. Y. Jen, Highly efficient all-inorganic perovskite solar cells with suppressed non-radiative recombination by a lewis base. *Nat.Commun.* **11**, 177 (2020).

54. M. Kaltenbrunner, G. Adam, E. D. Glowacki, M. Drack, R. Schwodiauer, L. Leonat, D. H. Apaydin, H. Groiss, M. C. Scharber, M. S. White, N. S. Sariciftci, S. Bauer, Flexible high power-per-weight

perovskite solar cells with chromium oxide-metal contacts for improved stability in air. *Nat. Mater.* **14**, 1032–1039 (2015).

55. S. P. Harvey, J. Messinger, K. Zhu, J. M. Luther, J. J. Berry, Investigating the effects of chemical gradients on performance and reliability within perovskite solar cells with TOF-SIMS. *Adv. Energy Mater.* **10**, 1903674 (2020).

56. J. Cao, S. X. Tao, P. A. Bobbert, C. P. Wong, N. Zhao, Interstitial occupancy by extrinsic alkali cations in perovskites and its impact on ion migration. *Adv. Mater.* **30**, 1707350 (2018).

57. W. E. I. Sha, H. Zhang, Z. S. Wang, H. L. Zhu, X. Ren, F. Lin, A. K. Y. Jen, W. C. H. Choy, Quantifying efficiency loss of perovskite solar cells by a modified detailed balance model. *Adv. Energy Mater.* **8**, 1701586 (2018).

58. H. Zhang, J. Cheng, F. Lin, H. He, J. Mao, K. S. Wong, A. K. Jen, W. C. Choy, Pinhole-free and surface-nanostructured NiO_x film by room-temperature solution process for high-performance flexible perovskite solar cells with good stability and reproducibility. *ACS Nano* **10**, 1503–1511 (2016).

59. Q. Cao, Z. Li, J. Han, S. J. Wang, J. Zhu, H. Tang, X. Li, X. Li, Electron transport bilayer with cascade energy alignment for efficient perovskite solar cells. *Sol. RRL* **3**, 1900333 (2019).

60. S. Wang, Z. Li, Y. Zhang, X. Liu, J. Han, X. Li, Z. Liu, S. Liu, W. C. H. Choy, Water-soluble triazolium ionic-liquid-induced surface self-assembly to enhance the stability and efficiency of perovskite solar cells. *Adv. Funct. Mater.* **29**, 1900417 (2019).

61. H. Tan, A. Jain, O. Voznyy, X. Lan, F. P. G. de Arquer, J. Z. Fan, R. Quintero-Bermudez, M. Yuan, B. Zhang, Y. Zhao, F. Fan, P. Li, L. N. Quan, Y. Zhao, Z.-H. Lu, Z. Yang, S. Hoogland, E. H. Sargent, Efficient and stable solution-processed planar perovskite solar cells via contact passivation. *Science* **355**, 722–726 (2017).

62. Y. Hou, X. Y. Du, S. Scheiner, D. P. McMeekin, Z. Wang, N. Li, M. S. Killian, H. W. Chen, M. Richter, I. Levchuk, N. Schrenker, E. Spiecker, T. Stubhan, N. A. Luechinger, A. Hirsch, P.

Schmuki, H.-P. Steinrück, R. H. Fink, M. Halik, H. J. Snaith, C. J. Brabec, A generic interface to reduce the efficiency-stability-cost gap of perovskite solar cells. *Science* **358**, 1192–1197 (2017).

63. J. A. Christians, P. Schulz, J. S. Tinkham, T. H. Schloemer, S. P. Harvey, B. J. Tremolet de Villers, A. Sellinger, J. J. Berry, J. M. Luther, Tailored interfaces of unencapsulated perovskite solar cells for >1,000 hour operational stability. *Nat. Energy* **3**, 68–74 (2018).

64. S.-H. Turren-Cruz, A. Hagfeldt, M. Saliba, Methylammonium-free, high-performance, and stable perovskite solar cells on a planar architecture. *Science* **362**, 449–453 (2018).

65. W. Chen, Y. Wu, Y. Yue, J. Liu, W. Zhang, X. Yang, H. Chen, E. Bi, I. Ashraful, M. Grätzel, L. Han, Efficient and stable large-area perovskite solar cells with inorganic charge extraction layers. *Science* **350**, 944–948 (2015).

66. Y. Wang, W. Chen, L. Wang, B. Tu, T. Chen, B. Liu, K. Yang, C. W. Koh, X. Zhang, H. Sun, G. Chen, X. Feng, H. Y. Woo, A. B. Djurišić, Z. He, X. Guo, Dopant-free small-molecule hole-transporting material for inverted perovskite solar cells with efficiency exceeding 21%. *Adv. Mater.* **31**, 1902781 (2019).